Chapter 3

Diagnostics of Super-flares Observed on Active Fast Rotator AB Doradus

This chapter analyzes intense X-ray flares observed on the active fast rotator AB Dor, utilizing data from XMM-Newton. A total of 21 flares are detected, and 13 strongest flares are analyzed in detail. The total X-ray energy of these flares is found to be in the range of 10^{34-36} *erg, in which the peak flare flux increased up to 34 times from the pre-/post-flaring states for the strongest observed flare. The duration of these flaring events is found in the range of 0.7 to 5.8 hrs. The quiescent state X-ray spectra are found to be explained by a three-temperature plasma with average temperatures of 0.29, 0.95, and 1.9 keV, respectively. The temperatures, emission measures, and abundances are found to vary during the flares. The peak flare temperature was found in the 31-89 MK range, whereas the peak emission measure was* $10^{52.5-54.7}$ cm^{-3} *. The abundances vary during the flares and increase by a factor of ~3 from the quiescent value for the strongest detected flare. The variation in individual abundances follows the inverse-FIP effect in quiescent and flare phases. The X-ray light curves of AB Dor are found to exhibit rotational*

modulation. The semi-loop lengths of the flaring events are derived in the range of $10^{9.9-10.7}$ cm, whereas the minimum magnetic field to confine the plasma in the flaring loop is estimated between 200 and 700 G. This chapter is devoted to analyses of intense X-ray flares detected on the active fast rotator AB Dor using observations from the XMM-Newton.

3.1 AB Dor

AB Dor A is a young, active, and a member of a pre-main-sequence quintuplet stellar system AB Doradus (=HD 36705) at a distance of 15.0 ± 0.1 pc (Guirado et al., 1997). The other companions, binaries AB Dor Ca/Cb (Climent et al., 2019) and AB Dor Ba/Bb (Vilhu and Linsky, 1987) are faint sources and are ignored in the following work. Hereafter, we refer to AB Dor A as AB Dor throughout the text. AB Dor is a highly active ultra-fast rotator of K0V spectral type with a rotational period of 0.5148 days (Pakull, 1981). It shows frequent flaring activity, probably due to its high spin rate (~50 times that of the Sun). Therefore, it possesses a strong magnetic field. It has a radius (R_*) of ~0.96 $R_\odot$, a mass of 0.86 $M_\odot$, and a surface temperature of 5081 K(see Guirado et al., 2011, and references therein). In the X-ray band, AB Dor has gained interest since its first detection by the Einstein Observatory (Pakull, 1981). AB Dor is observed by almost every X-ray satellite because of its X-ray brightness and positional advantage (galactic latitude ~-33°). Kuerster et al. (1997) studied long-term X-ray activities using ROSAT data and found no significant trend throughout five years. Almost all X-ray observatories have detected frequent flares in the corona of AB Dor. Vilhu et al. (1993) first reported statistical studies of X-ray flares, where they found a mean flare energy of $\sim 10^{34}$ erg, putting AB Dor as a frequent super-flaring star. In this context, we conducted a detailed study of X-ray flares on AB Dor using the XMM-Newton Observatory.

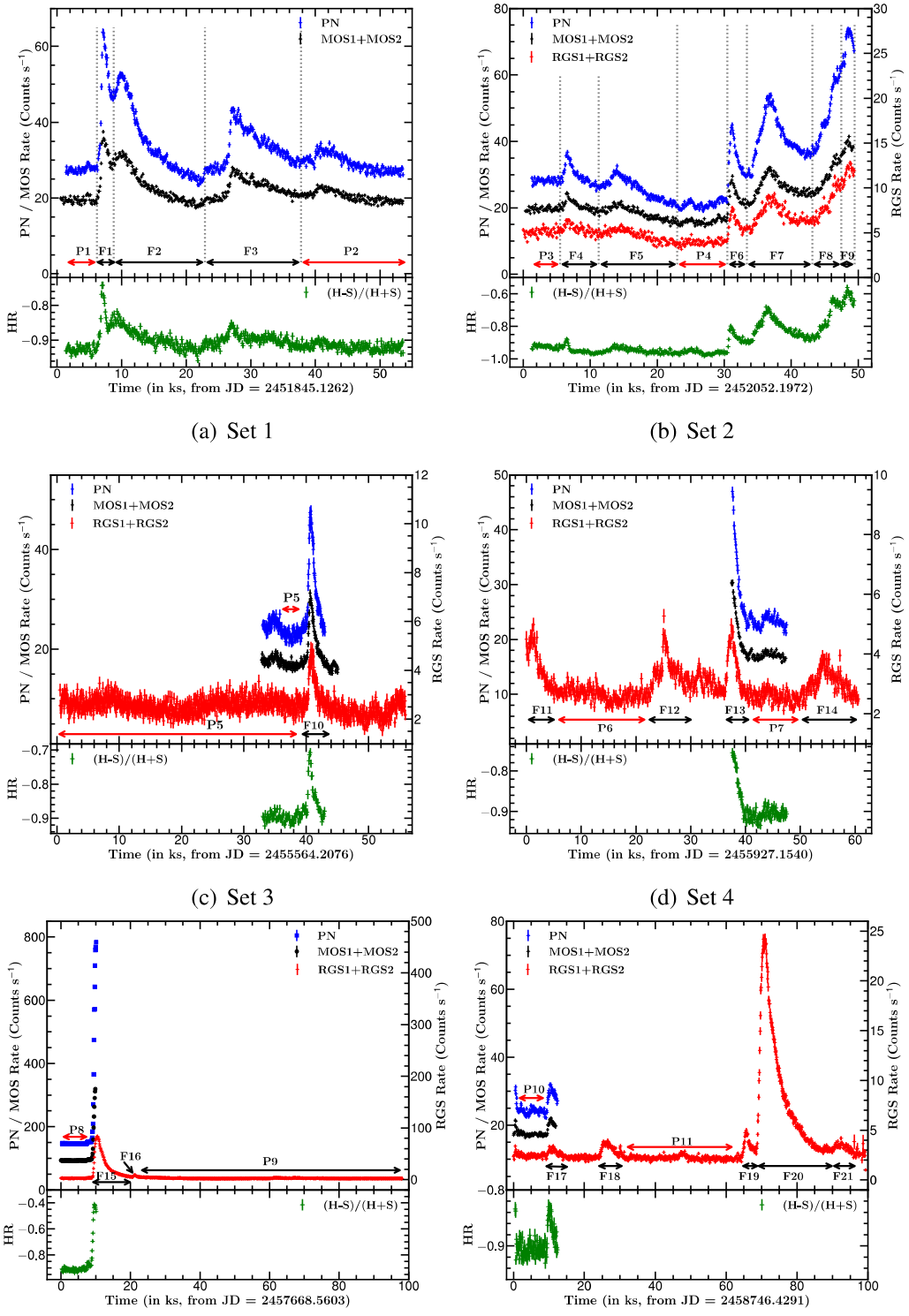

(a) Set 1 (b) Set 2

(c) Set 3 (d) Set 4

(e) Set 5 (f) Set 6

Figure 3.1: The background subtracted X-ray light curves of AB Dor for different observation epochs. Light curves from PN, MOS, and RGS detectors are shown in blue, black, and red colors, respectively. In order to plot the light curves from all three detectors in the same panel, the MOS count rates are scaled up as 0.8 × MOS for sets S1 and S2, 5+MOS for sets S3, S4, and S6, and 80+MOS for set S5. PN count rate is scaled up as 120+PN for set S5 and RGS count rate is scaled up as 1.8 × RGS for set S2.

Parameters	Value
RA	5h 28m 44.975s
DEC	-65° 26' 52.662″
Distance	14.85 pc
R_*	~0.96 $R_\odot$
M_*	~0.86 $M_\odot$
P_{Rot}	0.5148 days

Table 3.1: Basic parameters of AB Dor.

3.2 Observations and Data Reduction

The log of observation of the total six data sets from S1 to S6, which are analyzed in this chapter, is given in Table 2.1, and the standard data reduction procedure applied to these data sets is discussed in Chapter 2. Out of these datasets, S3 and S5 showed the presence of pile-up. To remove that, we chose annulus regions with inner and outer radii of 7.5" and 55", and 20" and 68", respectively, as mentioned in Table 2.1. However, all datasets were found to be free of proton flare events for energies exceeding 10 keV.

3.3 Analysis and Results

3.3.1 X-ray Light Curves

The upper panels of Fig. 3.1 show the background-subtracted X-ray light curves of AB Dor as obtained from EPIC and RGS instruments in the energy range of 0.3 – 10 keV and 0.33 – 2.07 keV, respectively, whereas the lower panels show the variation of hardness ratio (HR) with time, which is defined as (H-S)/(H+S), where H is the count rate in the hard energy band of 2.0 – 10.0 keV and S is the count rate in the soft energy band of 0.3 – 2.0 keV.

The X-ray light curves of AB Dor also exhibit rotational modulations (e.g., Collier Cameron et al., 1988; Kuerster et al., 1997; Vilhu et al., 1993). Therefore, we used HR as a proxy to detect flaring events. We considered excursions greater than three times the

standard deviation in the positive count rate from the pre/post-flare light curves to identify flares. Flaring regions in the light curves were identified when HR increased and mimicked the flare light curve. Using this approach, we detected 21 flares during the observations used here. We marked all the identified flare durations as Fi (where i = 1, 2, ... 21) in Fig. 3.1. Regions of constant HR beyond the flaring region of the light curves were identified as either pre or post-flare epochs and were marked by Pi (where i = 1, 2, ... 11) in the same figure. During the pre-/post-flare segments, HR remained almost constant. We fitted the following equation to model the light curve: the pre/post-flare segments were fitted with a horizontal straight line, and the rise and decay phases of the flares were fitted with an exponential function.

$$c(t) = \begin{cases} c_0, & \text{for } t \leq t_0 \\ c_0 \exp(\frac{t-t_p}{\tau_r}), & \text{for } t_0 \leq t \leq t_p \\ c_0 \exp(-\frac{t-t_p}{\tau_d}), & \text{for } t \geq t_p \end{cases} \tag{3.1}$$

Where c(t) is the time-dependent variation in count rate during the light curve, c_0 is the constant count rate during the quiescent state, t_0 and t_p denote the flare start time and flare peak time, respectively, and τ_r and τ_d are the e-folding rise and decay times of the flare. In the case of sets S2, S3, S4, and S5, the rotational modulation appears to be present as both pre-flare and post-flare states were observed at the different quiescent levels. Therefore, to account for the rotational modulation, we have fitted a sine wave with a period equal to the rotational period of AB Dor on the quiescent part of the light curve for sets S2, S4, and S5. However, in the case of set S3, we have fitted a sine wave with a period half of the rotational period of AB Dor, which can occur due to the presence of two persistent active longitudes separated by 180° (e.g. Berdyugina and Usoskin, 2003). After removing the rotational modulation from the original light curve, we applied the mentioned flare model fitting. Fig. 3.2 displays the fitted sine wave, the original light curves, and the fitted flare

Table 3.2: The best-fit model parameters for all the detected flares. Here, F/Q represents the ratio of the flare peak count rate to the quiescent count rate.

Parameters(→) Segments(↓)	τ_r (ks)	τ_d (ks)	F/Q	Parameters(→) Segments(↓)	τ_r (ks)	τ_d (ks)	F/Q
S1-F1	0.27±0.01	3.01±0.08	2.34±0.04	F12	1.1±0.1	1.3 ±0.2	2.00±0.09
F2	0.43±0.06	3.7 ±0.2	1.93±0.03	F13	0.50±0.05	1.02±0.07	1.89±0.09
F3	0.83±0.04	6.7 ±0.2	1.59±0.03	F14	1.2±0.2	2.9 ±0.3	1.49±0.08
S2-F4	0.35±0.05	0.9 ±0.1	1.30±0.03	S5-F15	0.52±0.02	2.19±0.05	34.4±0.4
F5	0.8 ±0.1	2.2 ±0.2	1.16±0.03	F16	0.66±0.06	0.92±0.04	3.5±0.1
F6	0.36±0.02	0.84±0.05	1.60±0.03	S6-F17	0.8±0.1	1.97±0.20	1.53±0.09
F7	2.19±0.08	2.9 ±0.1	2.56±0.04	F18	0.84±0.07	2.5 ±0.2	1.79±0.09
F8	0.42±0.08	0.7 ±0.2	2.84±0.05	F19	0.51±0.04	1.9 ±0.1	2.3±0.1
F9	2.99±0.08	6.0 ±1.0	3.50±0.05	F20	0.96±0.02	4.39±0.06	11.0±0.2
S3-F10	0.36±0.05	1.09±0.09	2.00±0.05	F21	4.9±0.9	2.4 ±0.3	1.9±0.1
S4-F11	2.9 ±0.7	1.28±0.09	1.89±0.09				

model applied to the residual light curves. In the instance of set S1, we could not confirm the presence of rotational modulation, likely because the quiescent state was absent due to frequent flaring events occurring throughout the observation. Conversely, in the case of S6, significant rotational modulation was not detected.

We have used the data obtained from the PN detector to model the light curves for sets S1 and S2. However, RGS data was used for sets S3, S4, S5, and S6 because the PN detectors do not cover the entire observation for these sets. The best-fit model parameters for all the 21 detected flares are shown in Table 3.2. The strength of these flares can be inferred from the quiescent to peak count rate ratio as mentioned in Table 3.2 by the parameter F/Q. The observed values of F/Q in AB Dor vary from ~1.2 to ~34, with most flares having F/Q of 2 – 4.

3.3.2 EPIC Spectral Analysis

In this section, we delve into an extensive discussion of the spectral analysis conducted on X-ray data from AB Dor, using observations from XMM-Newton. We employed time-resolved spectroscopy (TRS) to monitor changes in the X-ray spectral parameters throughout the observations. To begin, we isolated the flare components from the rest of the light curves. From the remaining light curve, we selected segments with the lowest mean

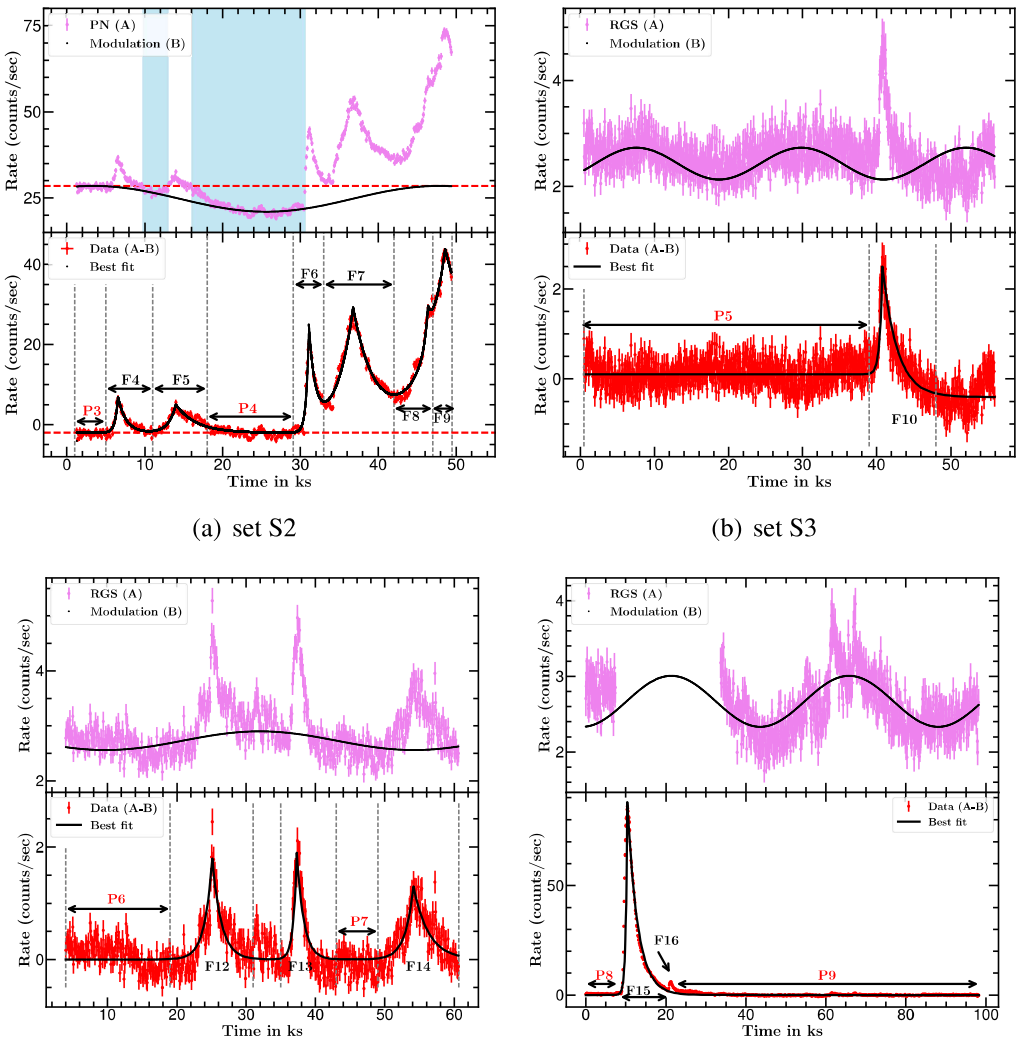

(a) set S2 (b) set S3

(c) set S4 (d) set S5

Figure 3.2: In the upper panels, PN/RGS light curve (A) and the presence of rotational modulation with best-fit sin curve (B) are shown in violet and black, respectively, for sets S2, S3, S4, and S5. To show the rotational modulation in set S5, the flare part is not shown due to the very high count rate during this flare, F15. The best-fit flare model on the residual (A-B) is shown in the lower panel in black. The regions shaded in light blue color in the upper panel of (a) represent the dimming areas as defined by (Veronig et al., 2021), and the red dotted lines show the level of pre-flare average counts.

count rates as pre- and/or post-flare segments, enabling us to identify the true quiescent state.

Our selection of 13 flares (F1-10, F13, F15, and F20 from RGS) out of the 21 total flares for time-resolved spectroscopy depended on the data available from the PN detector, which provided better statistics for low-exposure spectra. Furthermore, each flare was subdivided into multiple time bins, ensuring that each bin contained a similar and adequate number of counts for the subsequent spectral analysis.

3.3.2.1 The quiescent spectroscopy

We began by selecting the pre-/post-flare segments as proxies for the quiescent state in each observation and extracted the corresponding spectra. Fig. 3.3 showcases the quiescent state spectra of AB Dor from various observations. These X-ray spectra exhibited variations not only between different observations but also within a single observation. For instance, P3 and P4, both from the same observation, demonstrated inconsistency (refer also to Table 3.3).

To comprehend these variations, we conducted a comprehensive X-ray spectral analysis to determine parameters such as plasma temperature, emission measure, and abundance during these events. The quiescent state spectra were subjected to fitting with one (1-T), two (2-T), and three (3-T) temperature plasma models using APEC (Smith et al., 2001). We incorporated the X-ray absorption model PHABS to account for hydrogen column density (N_H), while solar photospheric abundances ($Z_\odot$) were adopted from Anders and Grevesse (1989). During spectral fitting, all temperatures, emission measures, and global abundances (Z) remained free parameters.

For N_H , we fixed it at the maximum value of galactic N_H , which is 2×10^{18} cm^{-2} for AB Dor. This value of N_H was computed based on the maximum E(B-V) value of 0.0003 mag for AB Dor (Boro Saikia et al., 2018) using the relation from Gorenstein (1975). The

3-T model exhibited a significantly better fit than the 1-T and 2-T models. The addition of another thermal component did not yield further improvement in the χ^2, and the parameters of the fourth component were not well constrained.

Table 3.3 summarizes the best-fit model parameters along with their reduced χ^2 values for all the quiescent state spectra from P1 to P10. We calculated the average values of temperature (TQA) and emission measures (EMQA) for each segment using the following formulas:

$$T_{QA} = \frac{\sum_{i=1}^{N} T_i EM_i}{\sum_{i=1}^{N} EM_i}; \quad EM_{QA} = \frac{1}{N} \sum_{i=1}^{N} EM_i, \tag{3.2}$$

Where N (=3) represents the number of plasma components in the 3T models. The calculated average values of TQA and EMQA were 0.94 ± 0.06 keV and 4.6 ± 0.7 × 10^{52} cm^{-3} , respectively. These average values exhibited consistency within a 2 σ level (refer to Table 3.3). The X-ray luminosity (L_{XQ}) was found to be variable, indicating varying coronal active regions from one observation to another.

3.3.2.2 Spectral evolution during the flares

To trace the evolution of spectral parameters during flares, we divided the full flare light curve into several time segments consisting of the rising, peak, and decay phases and generated spectra for each segment. The rising, peak, and decay phases are denoted by Ri, P, and Di, respectively. Here, i = 1,2..... The length of each segment was chosen in such a way that each segment contained an equal number of counts. The TRS was conducted on all available flares using the PN detector due to its high signal-to-noise ratio. Additionally, TRS was performed for flare F20 due to high count rates in the RGS spectra.

The X-ray spectra of flaring segments were also fitted with a 3-T APEC model. All the parameters of the 3-T APEC model were kept free during the spectral fitting. The first two temperatures were found to be constant within a 1σ level and were similar to

Table 3.3: Best fit spectral parameters from the pre/post-flare spectra using 3-T APEC model for all data sets.

Para (→) Seg (↓)	kT_1	kT_2	kT_3	T_{QA}	EM_1	EM_2	EM_3	EM_{QA}	Z ($Z_\odot$)	L_{XQ}	χ^2_ν (dof)
P1	$0.297^{+0.006}_{-0.006}$	$0.98^{+0.01}_{-0.01}$	$2.2^{+0.2}_{-0.2}$	$0.90^{+0.05}_{-0.04}$	$5.4^{+0.2}_{-0.2}$	$6.6^{+0.5}_{-0.5}$	$2.1^{+0.4}_{-0.3}$	$4.7^{+0.2}_{-0.2}$	$0.18^{+0.01}_{-0.01}$	$1.165^{+0.005}_{-0.005}$	1.27 (403)
P2	$0.288^{+0.003}_{-0.002}$	$0.974^{+0.006}_{-0.005}$	$1.99^{+0.04}_{-0.04}$	$1.0^{+0.01}_{-0.01}$	$4.8^{+0.1}_{-0.1}$	$6.3^{+0.2}_{-0.2}$	$3.6^{+0.1}_{-0.1}$	$4.90^{+0.08}_{-0.08}$	$0.194^{+0.005}_{-0.005}$	$1.277^{+0.002}_{-0.002}$	1.79 (742)
P3	$0.287^{+0.008}_{-0.007}$	$0.97^{+0.01}_{-0.01}$	$2.1^{+0.3}_{-0.1}$	$0.95^{+0.06}_{-0.04}$	$4.6^{+0.2}_{-0.2}$	$6.9^{+0.6}_{-0.4}$	$2.5^{+0.3}_{-0.4}$	$4.7^{+0.2}_{-0.2}$	$0.19^{+0.01}_{-0.01}$	$1.214^{+0.005}_{-0.005}$	1.03 (434)
P4	$0.282^{+0.007}_{-0.006}$	$0.94^{+0.02}_{-0.02}$	$1.8^{+0.2}_{-0.1}$	$0.85^{+0.05}_{-0.04}$	$3.7^{+0.2}_{-0.2}$	$4.0^{+0.4}_{-0.3}$	$1.8^{+0.3}_{-0.3}$	$3.2^{+0.2}_{-0.2}$	$0.20^{+0.02}_{-0.01}$	$0.863^{+0.004}_{-0.004}$	1.54 (361)
P5	$0.298^{+0.01}_{-0.008}$	$0.96^{+0.02}_{-0.02}$	$2.0^{+0.1}_{-0.1}$	$1.03^{+0.04}_{-0.04}$	$4.3^{+0.3}_{-0.3}$	$5.7^{+0.6}_{-0.5}$	$3.7^{+0.4}_{-0.4}$	$4.6^{+0.3}_{-0.2}$	$0.21^{+0.02}_{-0.02}$	$1.251^{+0.007}_{-0.007}$	1.07 (356)
P7	$0.278^{+0.005}_{-0.005}$	$0.86^{+0.02}_{-0.02}$	$1.5^{+0.1}_{-0.1}$	$0.97^{+0.05}_{-0.05}$	$3.5^{+0.2}_{-0.2}$	$3.6^{+0.3}_{-0.3}$	$5.3^{+0.3}_{-0.3}$	$4.1^{+0.2}_{-0.2}$	$0.23^{+0.02}_{-0.01}$	$1.07^{+0.01}_{-0.01}$	1.68 (523)
P8	$0.282^{+0.006}_{-0.007}$	$0.97^{+0.01}_{-0.01}$	$1.9^{+0.2}_{-0.1}$	$0.89^{+0.05}_{-0.03}$	$5.8^{+0.3}_{-0.3}$	$7.4^{+0.6}_{-0.6}$	$2.9^{+0.4}_{-0.4}$	$5.4^{+0.3}_{-0.3}$	$0.21^{+0.01}_{-0.01}$	$1.411^{+0.006}_{-0.006}$	1.29 (412)
P10	$0.270^{+0.004}_{-0.004}$	$0.952^{+0.008}_{-0.008}$	$1.9^{+0.1}_{-0.1}$	$0.91^{+0.03}_{-0.03}$	$5.9^{+0.2}_{-0.2}$	$6.9^{+0.3}_{-0.3}$	$3.6^{+0.2}_{-0.2}$	$5.5^{+0.1}_{-0.1}$	$0.18^{+0.01}_{-0.01}$	$1.346^{+0.004}_{-0.004}$	1.28 (546)
Avg	0.29±0.01	0.95±0.04	1.9±0.2	0.94±0.06	4.8±0.9	6±1	3±1	4.6±0.7	0.20±0.02	1.200±0.2	

Note: The first row and first column represent the parameters (para) and light curve segments (seg). All the temperatures and emission measures are in units of keV and 10^{52} cm^{-3} , respectively, whereas X-ray luminosity (L_{XQ}) is in units of 10^{30} erg s^{-1} . The error in the average values of the parameters in the last row is the standard deviation. The dof is the number of degrees of freedom, and χ^2_ν is the reduced χ^2.

the quiescent temperatures. However, the third temperature was found to be varying during the flare. Therefore, for further spectral fitting, we have fixed the first two temperatures and corresponding normalizations at the quiescent level and N_H at 2×10^{18} cm^2. Other parameters like Z, the temperature of the third component, and the corresponding normalization were kept free.

We have also fitted the spectra with the 3+1-T APEC model, fixing all the parameters of the first three components to the nearest quiescent state value and varying parameters of the fourth component. This model either does not constrain the model parameter or does not improve the statistics of the spectral fit. Therefore, we opted for the previous model for further analysis. All the best-fit spectral parameters with 68% confidence range and reduced χ^2 are given in Table 3.5, and the temporal variation of all these parameters is shown in Fig. 3.4.

The top panels of Fig. 3.4 depict the temporal evolution of the third temperature T3, which shows that the flare temperature is maximum during the rising phase of the flare. The

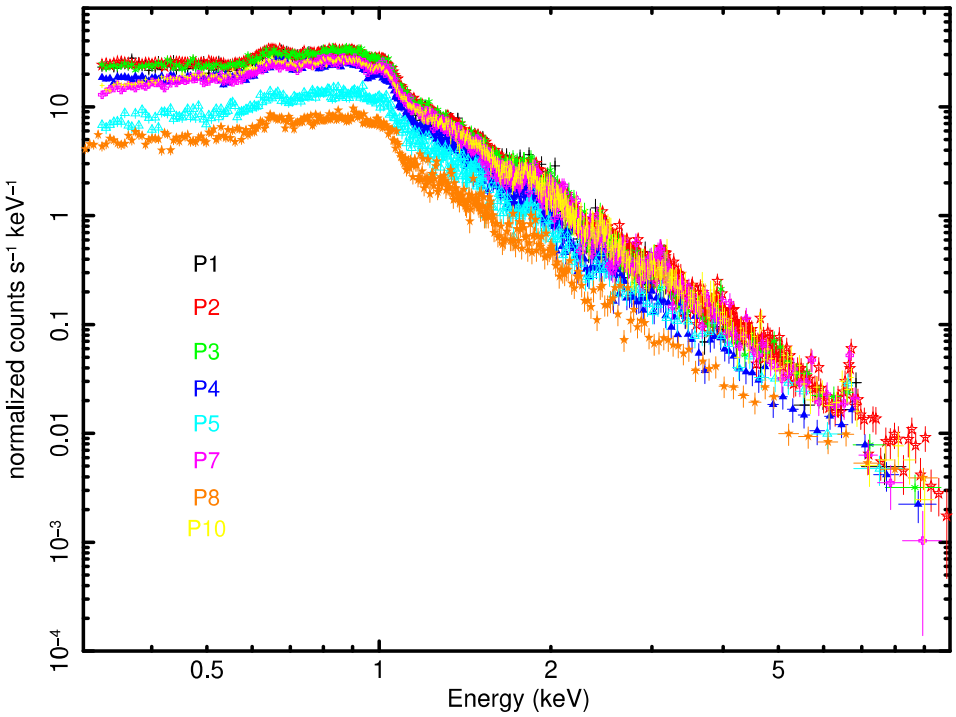

Figure 3.3: The X-ray spectra of pre- and post-flare states of AB Dor as obtained from the EPIC-PN detector.

T3 reached a value of 7.7 keV during the flare F15, the highest of all the flares analyzed here. The maximum flare temperature T3 ranges from 2.7 to 3.8 keV for the rest of the flares. Also, we have found in the case of multiple flares (flares F1 and F2 from set S1 and flares F6 to F9 from set S2), the temperature during the decay phase of the flare is increasing rather than decreasing. This discrepancy can be attributed to the overlap between the decay phase of the first flare and the rising phase of the second flare. Within this overlapping region, the heating generated during the ascending phase of the second flare influences the cooling or decay phase of the preceding flare. Consequently, this overlapping effect leads to an overall increase in temperature. Further, the variation in emission measure EM_3, abundance Z, and X-ray luminosity L_{XF} are found to be in agreement with the standard flare model and are shown in the second, third, and fourth plots of Figures 3.4 (a) to (f). The values of peak EM_3, Z, and L_{XF} were also found to be maximum for the flare F15

as 4.91×10^{54} cm^{-3} , 0.54 $Z_{\odot}$, and >42.4×10^{31} erg s^{-1} , respectively, whereas for the remaining flares the peak EM_3, Z and L_{XF} were found to be in the range of 3.2×10^{52} – 1.3×10^{54} cm^{-3} , 0.22 – 0.33 $Z_{\odot}$, and $0.9 - 3.6 \times 10^{31}$ erg s^{-1} , respectively.

3.3.3 Loop Modeling

Although stellar flares cannot be resolved spatially, their analogies with solar flares and loop models help us to infer the morphology and physical size of flaring loops and stellar corona. Observations of stellar flares do not always cover the entire duration of flares. In some cases, the rising phase is not covered, and in other cases, the decay phase is not observed. Also, in some flares, there is an overlap between the decaying phase of one flare and the rising phase of the other. In our case, only the decay phase of flare F13 and the rising phase of flare F15 are observed with the PN detector. So, the separate calculations for loop length from flare rise (Reale, 2007) and decay phases (Reale et al., 1997) have been made using the Hydrodynamic loop model. This model assumes a single dominant coronal loop, which includes plasma cooling as well as the heating effect during flare decay. We have determined the semi-loop length (L) using both of the approaches outlined below.

3.3.3.1 The rise phase

Reale (2007) introduced a detailed model for loop length calculation using the rise and peak phases of the stellar X-ray flare. As a consequence of the heating event, the loop's temperature experiences a rise, reaching its maximum at temperature T_0. Concurrently, due to chromospheric evaporation, the density also rises and peaks at temperature T_M within the flaring loop. During the peak phase, heating stops and conduction cooling starts to dominate, which causes the temperature to drop at the peak phase. At this stage, the continuous increase in density indicates the ongoing evaporation process.

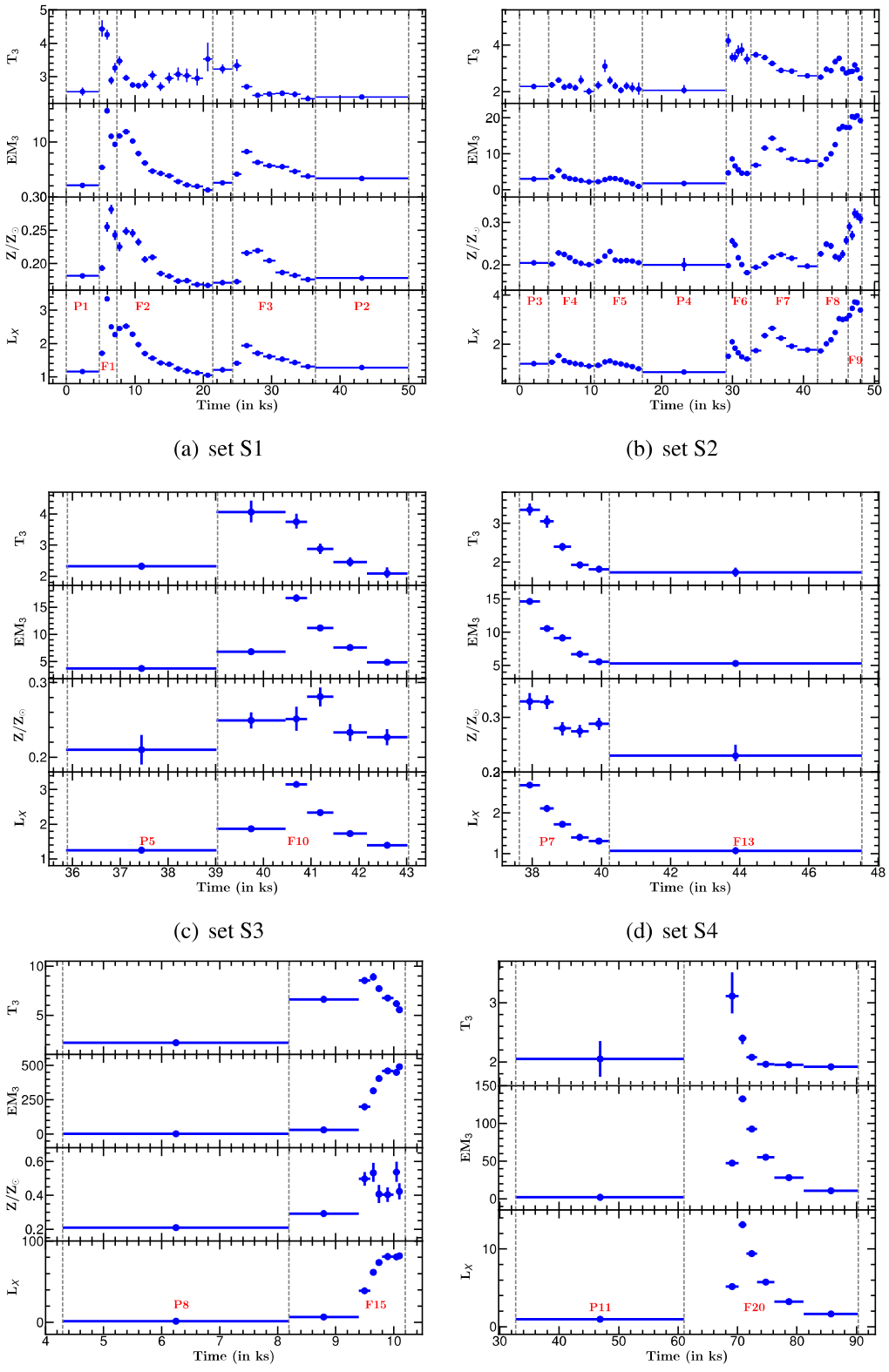

(a) set S1 (b) set S2

(c) set S3 (d) set S4

(e) set S5 (f) set S6

Figure 3.4: Temporal evolution of the spectral parameters of AB Dor during flares and quiescent states, where top to bottom plots show the variation of temperature (T_3) in units of 10^7 K, emission measure (EM_3) in units of 10^{52} cm^{-3} , relative abundance (Z/Z$_\odot$), and X-ray luminosity in units of 10^{30} erg s^{-1} .

Using hydrodynamic simulations of semi-circular flaring loops with constant cross-section, Reale (2007) derived an empirical formula for semi-loop length as

$$L_r = 950 \frac{T_0^{5/2}}{T_M^2} t_M \ \text{cm} \tag{3.3}$$

Where L_r is the semi-loop length in units of cm, T_0 and T_M are the maximum temperature and temperature at maximum density, respectively, in units of K, and t_M is the time at which density maximum occurs in units of sec. The derived semi-loop lengths using this model are given in Table 3.4 and were found to be in the range of $0.8 - 4.5 \times 10^{10}$ cm. The largest loop length was found for flare F15, whereas the smallest loop length was found for flares F1, F6, and F9.

3.3.3.2 The decay phase

Considering pure cooling during the decay phase of the flare, Serio et al. (1991) derived a single coronal loop length using thermodynamic cooling time scales. Further, Sylwester et al. (1993) explained the sustained heating during the decay of a spatially resolved solar flare by introducing the slope in the density-temperature diagram. In the process of explaining the slower decay, Reale et al. (1997) included the effect of significant heating during flare decay using a time-dependent hydrodynamic loop model and added a correction factor $F(\zeta)$ to the derived half loop length (L_d) as shown in the following equation.

$$L_d = 2.7 \times 10^3 \frac{\tau_d T_{max}^{1/2}}{F(\zeta)} \ \text{cm} \quad \text{for} \quad 0.35 < \zeta \leq 1.6 \tag{3.4}$$

$$\text{with} \ \ T_{max} = 0.13 T_0^{1.16}, \quad F(\zeta) = \frac{0.51}{\zeta - 0.35} + 1.36 \tag{3.5}$$

Here, ζ is the slope of the $\log(\sqrt{(EM)})$ versus log(T) diagram (equivalent to density – temperature diagram) during the decay phase of the flare. This diagram is shown in Fig.

3.5 for the flares F7, F10, F13, and F20, along with the best-fit straight line. The T_0 is the maximum best-fit temperature derived from the spectral fitting of the data in units of K. The F(ζ) in equation 3.5 is valid for the observation from the EPIC instruments. A similar F(ζ) relation was adopted for observations from the RGS instrument (private communication with Reale F.). The slope (ζ) of the log($\sqrt{EM}$) vs log(T) curve is found to be 0.5±0.1, 0.9±0.1, 1.4 ± 0.2, and 0.21 ± 0.05 for flares F7, F10, F13, and F20, respectively. The low values of ζ indicate the presence of sustained heating during the decay of these flares. For the flare F20, the value of ζ is out of the range of the model. Therefore, loop length could not be derived from the decay method for F20. For the other flares where the decay phase was observed, we could not use this method as another flare emerged during the decay phase of the previous flare. This situation prevented us from tracing the density-temperature path, which is crucial for determining the loop length. The derived loop lengths for these flares are also given in Table 3.4. These values of the loop lengths are well within 1σ of those derived from the flare rise method.

3.3.4 Loop Parameters

We have calculated the flaring loop volume (V) using the approach used in the past in the absence of direct measurement (see e.g. Maggio et al., 2000; Pandey and Singh, 2008) by using equation $V = 2\pi\beta^2 L^3$ cm^3, where β is the ratio of loop radius to the half loop length. From the solar case, we assume the values of β between 0.1 – 0.3 (Golub et al., 1980). For $\beta = 0.3$, the V is estimated to be in the range of $3 \times 10^{29} - 5 \times 10^{31}$ cm^3 and found to be maximum for flare F15 and minimum for flare F9. Using the values of V, T_{max}, and peak emission measure (EM), we have derived the plasma density (n_e), pressure (p) at the loop apex, and minimum magnetic field (B_{min}) required to confine the plasma inside the coronal loop. The total plasma density is a sum of electron and hydrogen ion densities (n_H). The

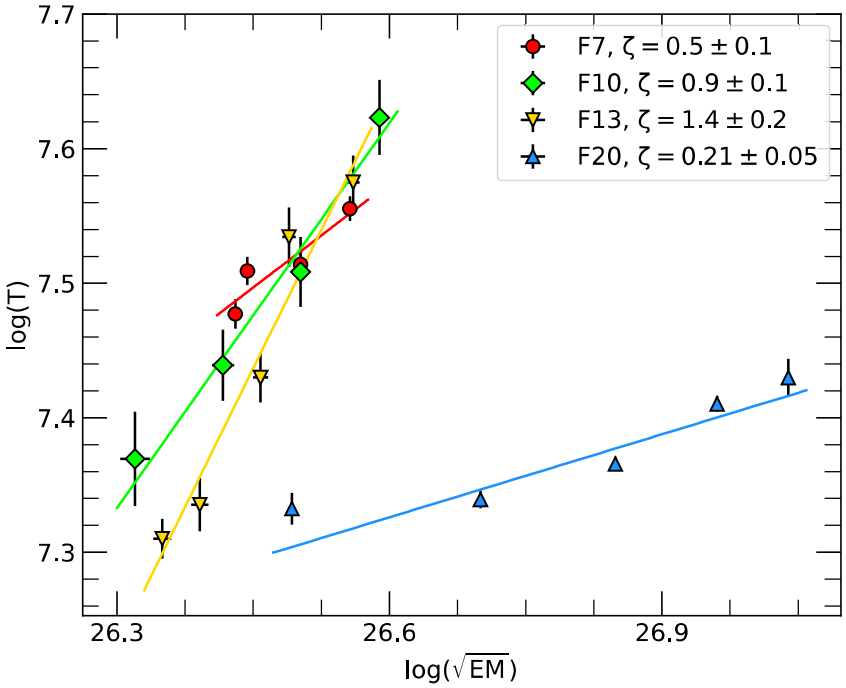

Figure 3.5: Flare evolution in the log $\sqrt{EM}$ versus log(T) curve during the decay phase for flares F7, F10, F13, and F20 along with the best fit straight line. The slope (ζ) of the decay path of log $\sqrt{EM}$ vs. log(T) is also given in the inset for each flare.

n_H is found to be 0.8 times n_e[1]. Thus the values of n_e, p, V and B_{min} are estimated as:

$$n_e = \sqrt{\frac{EM}{0.8V}} \text{ cm}^{-3}; \quad p = 1.8 n_e k T_{max} \text{ dyne cm}^{-2}; \quad B_{min} = \sqrt{8\pi p} \text{ G} \tag{3.6}$$

All the estimated values of V, n_e, p, and B_{min} are given in Table 3.4. The n_e was estimated in the range of 1 to 9×10^{11} cm^{-3}, whereas the p was estimated to be in the range of 0.2 to 2×10^4 dyne cm^{-2} for all the flares analyzed here. The B_{min} was within the range of 200 to 700 Gauss. Among the flares studied, the parameters p and B reached their highest values for flare F1, while the lowest values were observed for flare F5. In a scenario where β equals 0.1, these parameters would undergo transformations such that the V would become $\frac{V}{9}$, n_e would be $3n_e$, p would increase to $3p$, and B_{min} would change to $1.73B_{min}$.

[1]As $n_{He} = 0.1\ n_H$, hence $n_H/n_e = n_H/(n_H + 2n_{He}) = 1/1.2 = 0.833$

The estimated loop lengths were found to be much smaller than the pressure scale height[2] of the flaring plasma of AB Dor. Therefore, one can assume that the flaring loops are close to a steady-state condition. Thus, the RTV scaling law (Rosner et al., 1978b) can be applied for the estimation of the physical parameters of flaring plasma (see also Aschwanden et al., 2008).

The heating rate per unit volume (HR_V) at the flare peak can be estimated by the following RTV relationship:

$$HR_V \sim 10^{-6} T_{max}^{7/2} L^{-2} \tag{3.7}$$

Assuming the constant heating during the rise and decay phases of the flare, the total heating rate (E_{HR}) can be estimated as ($E_{HR} \sim HR_V \times V$). The total energy corresponding to the heating rate is calculated as $E_{H,Total} = E_{HR} \times (\tau_r + \tau_d)$. The estimated values E_{HR} and $E_{H,Total}$ are found to be in the range of $1 \times 10^{31} - 4 \times 10^{33}$ erg s^{-1} , and $3 \times 10^{34} - 1 \times 10^{37}$ erg, respectively. These parameters were found to be maximum for the strongest flare, F15, observed in the sample. Under the assumption that the energy released during a flare is of magnetic origin, we have calculated the total non-potential magnetic field (B_{Total}) within the active region of the star that corresponds to the release of flare energy. The B_{Total} is found to be in the range of 0.4 to 3.4 kG, as determined by the equation $E_{H,Total} = (B_{Total}^2 - B_{min}^2) \times V/8\pi$. For a comprehensive overview of all estimated loop parameters for AB Dor, please refer to Table 3.4.

3.4 Discussion and Conclusions

The quiescent level always exists in the stars even during the flare, so confining quiescent emission becomes much more important in studies of flares. We found that the quiescent corona of AB Dor can be well described by three temperature plasma models. In the

[2] $h_p = kT_{max}/\mu m_H g$, where k is Boltzmann's Constant, T_{max} is the maximum temperature, μ is mean molecular weight, m_H is the mass of a hydrogen atom and g is surface gravity of the star.

Table 3.4: Loop parameters.

Flare (→)	F1	F2	F3	F4	F5	F6	F7
Parameters (↓)							
L_{XF} (10^{31} erg s^{-1})	0.982±0.004	1.986±0.004	1.094±0.003	0.890±0.003	0.941±0.003	1.000±0.004	1.268±0.002
$E_{X,Total}$ (10^{34} erg)	3.20±0.08	8.2±0.4	8.2±0.2	4.1±0.3	4.4±0.3	1.17±0.06	7.0±0.2
t_M (ks)	1.2	1.35	2.1	1.45	2.25	0.9	3.05
T_0 (MK)	44±2	35±1	33±2	34±1	31±2	42±3	36±1
T_M (MK)	43±2	30±1	27±1	25±1	25±2	35±2	32±1
L_r (10^{10} cm)	0.8±0.1	1.0±0.1	1.8±0.2	1.5±0.2	1.8±0.4	0.8±0.2	2.2±0.2
L_d (10^{10} cm)	...	...	...	...	...	...	1.6±0.7
V (10^{29} cm^3)	3±1	6±2	30±13	21±8	33±22	3±2	57±16
n_e (10^{11} cm^{-3})	8±1	5.1±0.8	1.8±0.4	1.8±0.4	1.1±0.4	6±2	1.8±0.2
p (10^4 dyne cm^{-2})	2.0±0.4	0.9±0.1	0.32±0.07	0.32±0.06	0.17±0.06	1.4±0.5	0.33±0.05
B_{min} (G)	703±69	481±37	282±31	285±28	209±36	584±112	288±21
B_{Total} (kG)	3.4±0.6	1.9±0.2	1.3±0.2	1.3±0.2	0.9±0.2	1.9±0.5	1.1±0.1
E_{HR} (10^{31} erg s^{-1})	4±1	1.8±0.3	2.7±0.7	2.8±0.5	2.1±0.8	3±1	4.5±0.7
$E_{H,Total}$ (10^{34} erg)	13±3	8±1	20±5	13±3	10±4	4±1	25±4
M_{CME} (10^{18} g)	~2.52	~1.98	~2.07	~1.21	~0.97	~0.82	~2.57
Flare (→)	F8	F9	F10	F13	F15	F20	-
L_{XF} (10^{31} erg s^{-1})	1.750 ±0.005	1.743±0.006	1.048±0.006	>0.9[a]	>42.4[b]	3.62 ± 0.01	-
$E_{X,Total}$ (10^{34} erg)	2.0±0.3	12±2	1.5±0.1	>1.4[a]	>115[b]	19.4±0.3	-
t_M (ks)	3.55	1.3	1.675	...	1.95	2.85	-
T_0 (MK)	34±1	31±1	41±4	34±1	89±4	31±4	-
T_M (MK)	30±1	29±1	38±2	34±1	56±2	24±1	-
L_r (10^{10} cm)	2.6±0.3	0.8±0.1	1.2±0.3	...	4.5±0.5	2.5±0.7	-
L_d (10^{10} cm)	...	...	1.2±0.2	1.2±0.1	...	...	-
V (10^{29} cm^3)	104±35	2.9±0.9	9±7	10±2	515±172	88±74	-
n_e (10^{11} cm^{-3})	1.5±0.2	9±1	5±2	4.5±0.6	3.4±0.6	4±2	-
p (10^4 dyne cm^{-2})	0.26±0.05	1.5±0.2	1.0±0.4	0.8±0.1	1.9±0.3	0.7±0.3	-
B_{min} (G)	255±22	617±48	504±99	443±29	682±59	415±91	-
B_{Total} (kG)	0.4±0.1	2.5±0.4	1.4±0.4	1.0±0.1	2.3±0.3	0.8±0.3	-
E_{HR} (10^{31} erg s^{-1})	4.7±0.8	1.0±0.2	4±2	2.0±0.3	379±73	3±2	-
$E_{H,Total}$ (10^{34} erg)	5±1	7±2	6±3	3.0±0.5	1027±200	16±8	-
M_{CME} (10^{18} g)	~1.10	~3.51	~1.39	~1.33	~15.53	7.17	-

[a] Parameters derived using only the decay phase of the flare.
[b] Parameters derived using only the rise phase of the flare.

present study, the average values of T_{QA} and EM_{QA} are found to be 0.94 keV and 4.6×10^{52} cm^{-3} from APEC model, and 1.1 keV and 3.1×10^{52} cm^{-3} from VAPEC model, respectively. These values of T_{QA} and EM_{QA} are consistent with those from the earlier studies of AB Dor (e.g. Güdel et al., 2001; Sanz-Forcada et al., 2003). The quiescent state luminosity, L_{XQ} of AB Dor is not found to be constant for different observations analyzed here. It was found to be highest during P8 with a value of 1.4×10^{30}, erg s^{-1} whereas, during P4, the value of L_{XQ} of 0.9×10^{30} erg s^{-1} is found to be lowest.

We have performed a comprehensive study of the 13 strongest X-ray superflares out of a total of 21 observed flares on AB Dor using a large set of data sets from 2000 to 2019 with the XMM-Newton satellite. The time duration of these 21 flares ranges from ~0.7 to ~5.8 hrs. The e-folding rise and decay times of these flares are found to be in the range of 0.27 – 4.9 ks and 0.7 – 6.7 ks, respectively, which shows the rapid rise and slower decay pattern of the flares. This kind of trend has been found in many solar and stellar flares (Pandey and Singh, 2008, 2012; van den Oord et al., 1988; Yan et al., 2021). Similar to the flares observed in the past, the F/Q ratios of the flares observed are in the range of 2 – 4 (e.g. Güdel et al., 2001; Lalitha and Schmitt, 2013). In the present study, flares F15 and F20 have the highest values of F/Q of 34 and 11, respectively. Earlier two strongest X-ray flares were observed in 1997 by BeppoSAX with F/Q of ~100 (Maggio et al., 2000). These two X-ray flares from BeppoSAX appear to be the strongest flares observed thus far, and in our present data, the flares F15 and F20 appear to be the next two strongest flares observed in AB Dor thus far.

The detailed TRS analysis shows the variation in spectral parameters during the flaring events. The peak flare temperature was found to be in the range of 31 to 89 MK. Flares F5, F9, and F20 had the lowest peak temperatures, while flare F15 had the highest, and were ~3 to 8 times higher than the quiescent temperature. Whereas the peak emission measure was found to be in the range of 3.2 to 491×10^{52} cm^{-3} , in which the maximum value is found for flare F15. Based on the results of TRS, it has been observed that the flare temperature peaks during the rising phase, while the emission measure peaks during the peak phase of the flare. This type of delay between peak temperature and peak emission measure has also been found in many solar and stellar flares (Stelzer et al., 2002; Sylwester et al., 1993; van den Oord and Mewe, 1989). The reason behind this delay is the possible magnetic reconnection process, which leads to the particle acceleration and chromospheric evaporation process (Reale, 2007). The temporal variation in flare temperature of independent single flares

and multiple overlapped flares is found to be different. In the case of independent single flares, the temperature rises during the flare's rising phase and decreases during the decay phase due to conduction and radiative cooling. However, in multiple overlapped flares, the temperature remains either constant or increases during the decay phase, as the decay phase of one flare is overlapped with the rising phase of the next flare.

We have also traced the global coronal abundances during the flaring events and found them to be varying as the flare evolves. It is found to be peaked around the peak phase of the flare. We found a 1.1 to 2.7-fold increase in abundances from the quiescent state value (~0.2 $Z_{\odot}$) with a maximum increase in abundances for the strongest flare, F15. The enhancement in the coronal abundance during the flares could be related to an increase in density within the flaring loop of constant volume, which is indicative of a large amount of evaporation of chromospheric material inside the loop due to intense heating during the flares.

Using the hydrodynamic loop model, we have derived the semi-loop length of the flares and found it to be in the range of $0.8 - 4.5 \times 10^{10}$ cm. The estimated loop length is also found to be similar to the earlier observed flares on AB Dor (Güdel et al., 2001; Hussain et al., 2007; Lalitha et al., 2013; Mason et al., 2001). The highest loop length in AB Dor was found to be $\sim 8.8 \times 10^{10}$ cm in November 2009 observations (Lalitha et al., 2013). In the case of the Sun, the typical loop length is found to be of the order of 10^9 - 10^{10} cm (Mullan, 2009). The loop heights ($2L/\pi$) corresponding to semi-loop lengths of all these flaring events observed so far are 8 to 43% of the radius of AB Dor. The total energy released by the flares was estimated to be in the range of 3×10^{34} - 1×10^{37} erg, which is very large in comparison to the total energy of the strongest flares observed on the Sun (~10^{32} erg Emslie et al., 2012; Zimovets et al., 2020). Also, the total magnetic field of the loop is found to be around 0.4 - 3.4 kG, which is the typical magnetic field observed in AB Dor (Donati and Collier Cameron, 1997; Jardine et al., 1999).

If we closely inspect the PN light curve of the post-flare phase of set S2, we notice a continuous dimming as shown by Veronig et al. (2021). A rotational modulation appears in most X-ray light curves of AB Dor, possibly due to the stellar surface's eclipsing of the coronal active regions (Singh et al., private communication). After removing the effect of rotational modulation from set S2 and following the definition of dimming as given in Veronig et al. (2021), we didn't see any strong signature of such dimming in the light curve (See Fig. 3.2). An empirical relationship between the stellar flare energy in X-rays and its associated CME mass is estimated as $M_{CME}(g) = 10^{-1.5\pm0.5} E_G^{0.59\pm0.02}$, where E_G is the X-ray energy in GOES (1 – 8 Å) energy band (Aarnio et al., 2012; Drake et al., 2013). The derived X-ray flux is converted into GOES flux using WEBPIMMS for the derived flare temperatures of AB Dor as described in Section 3.3.2.2. The estimated values of M_{CME} for AB Dor are found to be in the range 10^{18-19} g and are found to be maximum for the flare F15. These values of CMEs are 10 to 100 times more than the most massive solar CME (Yashiro and Gopalswamy, 2009) and similar to other stellar CMEs (Gunn et al., 1994; Karmakar et al., 2022; Namekata et al., 2021).

Table 3.5: Best fit spectral parameters of each temporal segment of the flares F1-F10, F13, F15, and F20. Here, FS represents flare segments, and ST and ET refer to the start and end times, respectively, of each flare segment relative to the start time of the corresponding observation.

Set	Flare	FS	ST:ET (ks)	kT_3 (keV)	EM_3 (10^{52} cm^{-3})	Z ($Z_\odot$)	L_{XF} (10^{30} erg s^{-1})	χ^2_ν (dof)
S1	F1	R	4.8 : 5.7	$3.8^{+0.2}_{-0.2}$	$5.4^{+0.2}_{-0.2}$	$0.193^{+0.004}_{-0.005}$	$1.71^{+0.01}_{-0.01}$	1.1 (352)
		P	5.7 : 6.3	$3.7^{+0.1}_{-0.1}$	$15.7^{+0.3}_{-0.3}$	$0.255^{+0.007}_{-0.007}$	$3.34^{+0.02}_{-0.02}$	1.54 (426)
		D1	6.3 : 6.9	$2.49^{+0.09}_{-0.1}$	$11.0^{+0.3}_{-0.3}$	$0.281^{+0.007}_{-0.007}$	$2.5^{+0.02}_{-0.02}$	1.33 (350)
		D2	6.9 : 7.4	$2.8^{+0.1}_{-0.1}$	$9.6^{+0.3}_{-0.3}$	$0.243^{+0.007}_{-0.007}$	$2.27^{+0.02}_{-0.02}$	1.03 (317)
	F2	R	7.4 : 8.2	$3.0^{+0.1}_{-0.1}$	$11.1^{+0.3}_{-0.3}$	$0.225^{+0.007}_{-0.007}$	$2.45^{+0.02}_{-0.02}$	1.05 (360)
		P	8.2 : 9.3	$2.56^{+0.09}_{-0.07}$	$11.9^{+0.2}_{-0.3}$	$0.248^{+0.006}_{-0.006}$	$2.52^{+0.01}_{-0.01}$	1.0 (432)
		D1	9.3 : 10.1	$2.37^{+0.07}_{-0.07}$	$10.2^{+0.3}_{-0.3}$	$0.246^{+0.006}_{-0.006}$	$2.28^{+0.01}_{-0.01}$	0.98 (374)
		D2	10.1 : 11.0	$2.35^{+0.08}_{-0.08}$	$7.9^{+0.2}_{-0.2}$	$0.232^{+0.005}_{-0.005}$	$1.97^{+0.01}_{-0.01}$	1.16 (365)
		D3	11.0 : 12.0	$2.38^{+0.1}_{-0.09}$	$6.2^{+0.2}_{-0.2}$	$0.206^{+0.005}_{-0.005}$	$1.7^{+0.01}_{-0.01}$	1.29 (350)
		D4	12.0 : 13.2	$2.6^{+0.1}_{-0.1}$	$4.7^{+0.2}_{-0.2}$	$0.209^{+0.004}_{-0.004}$	$1.56^{+0.01}_{-0.01}$	1.08 (359)
		D5	13.2 : 14.4	$2.3^{+0.1}_{-0.1}$	$4.3^{+0.2}_{-0.2}$	$0.185^{+0.004}_{-0.004}$	$1.42^{+0.01}_{-0.01}$	1.05 (343)
		D6	14.4 : 15.7	$2.5^{+0.2}_{-0.1}$	$3.9^{+0.2}_{-0.2}$	$0.181^{+0.004}_{-0.004}$	$1.38^{+0.01}_{-0.01}$	1.1 (349)

Continued on next page

Table 3.5 – continued from previous page

Set	Flare	FS	ST:ET (ks)	kT_3 (keV)	EM_3 (10^{52} cm^{-3})	Z ($Z_\odot$)	L_{XF} (10^{30} erg s^{-1})	χ^2_ν (dof)
		D7	15.7 : 17.0	$2.6^{+0.2}_{-0.2}$	$2.8^{+0.2}_{-0.2}$	$0.174^{+0.004}_{-0.004}$	$1.24^{+0.01}_{-0.01}$	1.04 (330)
		D8	17.0 : 18.3	$2.6^{+0.2}_{-0.2}$	$2.2^{+0.1}_{-0.1}$	$0.174^{+0.003}_{-0.003}$	$1.17^{+0.01}_{-0.01}$	1.03 (336)
		D9	18.3 : 20.0	$2.5^{+0.2}_{-0.2}$	$1.9^{+0.1}_{-0.2}$	$0.169^{+0.003}_{-0.003}$	$1.12^{+0.01}_{-0.01}$	1.07 (328)
		D10	20.0 : 21.4	$3.0^{+0.4}_{-0.3}$	$1.3^{+0.1}_{-0.1}$	$0.167^{+0.003}_{-0.003}$	$1.05^{+0.01}_{-0.01}$	1.19 (310)
	F3	R	24.3 : 25.6	$2.9^{+0.2}_{-0.1}$	$4.2^{+0.2}_{-0.2}$	$0.173^{+0.004}_{-0.004}$	$1.41^{+0.01}_{-0.01}$	1.12 (358)
		P	25.6 : 27.2	$2.33^{+0.06}_{-0.08}$	$8.2^{+0.2}_{-0.2}$	$0.216^{+0.004}_{-0.004}$	$1.94^{+0.01}_{-0.01}$	1.35 (446)
		D1	27.2 : 28.8	$2.10^{+0.06}_{-0.06}$	$6.3^{+0.2}_{-0.2}$	$0.219^{+0.004}_{-0.004}$	$1.71^{+0.01}_{-0.01}$	1.26 (414)
		D2	28.8 : 30.6	$2.14^{+0.06}_{-0.06}$	$5.7^{+0.2}_{-0.2}$	$0.204^{+0.004}_{-0.004}$	$1.61^{+0.01}_{-0.01}$	1.14 (418)
		D3	30.6 : 32.6	$2.16^{+0.07}_{-0.06}$	$5.5^{+0.1}_{-0.1}$	$0.187^{+0.003}_{-0.003}$	$1.53^{+0.01}_{-0.01}$	1.2 (428)
		D4	32.6 : 34.3	$2.13^{+0.08}_{-0.07}$	$4.7^{+0.2}_{-0.2}$	$0.182^{+0.004}_{-0.004}$	$1.43^{+0.01}_{-0.01}$	1.0 (386)
		D5	34.3 : 36.4	$2.02^{+0.08}_{-0.07}$	$3.8^{+0.1}_{-0.1}$	$0.176^{+0.003}_{-0.003}$	$1.31^{+0.01}_{-0.01}$	1.02 (391)
S2	F4	R	4.1 : 5.1	$3.0^{+0.1}_{-0.1}$	$3.6^{+0.2}_{-0.2}$	$0.202^{+0.005}_{-0.005}$	$1.27^{+0.01}_{-0.01}$	1.28 (299)
		P	5.1 : 6.0	$2.15^{+0.1}_{-0.08}$	$5.4^{+0.2}_{-0.2}$	$0.228^{+0.006}_{-0.005}$	$1.54^{+0.01}_{-0.01}$	1.12 (334)
		D1	6.0 : 6.7	$1.89^{+0.1}_{-0.1}$	$3.7^{+0.2}_{-0.2}$	$0.224^{+0.006}_{-0.006}$	$1.33^{+0.01}_{-0.01}$	1.15 (281)

Continued on next page

Table 3.5 – continued from previous page

Set	Flare	FS	ST:ET (ks)	kT_3 (keV)	EM_3 (10^{52} cm^{-3})	Z ($Z_\odot$)	L_{XF} (10^{30} erg s^{-1})	χ^2_ν (dof)
		D2	6.7 : 7.5	$1.93^{+0.1}_{-0.1}$	$3.2^{+0.2}_{-0.2}$	$0.217^{+0.005}_{-0.005}$	$1.26^{+0.01}_{-0.01}$	1.09 (287)
		D3	7.5 : 8.3	$1.86^{+0.1}_{-0.1}$	$2.9^{+0.2}_{-0.2}$	$0.208^{+0.005}_{-0.005}$	$1.21^{+0.01}_{-0.01}$	1.16 (281)
		D4	8.3 : 9.1	$2.15^{+0.2}_{-0.2}$	$2.6^{+0.2}_{-0.2}$	$0.203^{+0.005}_{-0.005}$	$1.18^{+0.01}_{-0.01}$	1.26 (279)
		D5	9.1 : 10.5	$1.73^{+0.1}_{-0.1}$	$2.2^{+0.2}_{-0.2}$	$0.2^{+0.005}_{-0.005}$	$1.11^{+0.01}_{-0.01}$	1.11 (276)
	F5	R1	10.5 : 11.7	$1.96^{+0.2}_{-0.1}$	$2.2^{+0.2}_{-0.2}$	$0.208^{+0.005}_{-0.005}$	$1.14^{+0.01}_{-0.01}$	1.03 (262)
		R2	11.7 : 12.4	$2.66^{+0.2}_{-0.2}$	$2.8^{+0.2}_{-0.2}$	$0.22^{+0.005}_{-0.005}$	$1.28^{+0.01}_{-0.01}$	1.08 (265)
		P	12.4 : 13.1	$2.14^{+0.2}_{-0.1}$	$3.2^{+0.2}_{-0.2}$	$0.231^{+0.006}_{-0.006}$	$1.32^{+0.01}_{-0.01}$	1.11 (264)
		D1	13.1 : 13.9	$1.93^{+0.1}_{-0.1}$	$3.1^{+0.2}_{-0.2}$	$0.211^{+0.006}_{-0.006}$	$1.24^{+0.01}_{-0.01}$	1.06 (275)
		D2	13.9 : 14.7	$1.78^{+0.1}_{-0.1}$	$2.8^{+0.2}_{-0.2}$	$0.209^{+0.006}_{-0.006}$	$1.2^{+0.01}_{-0.01}$	1.09 (267)
		D3	14.7 : 15.5	$1.93^{+0.1}_{-0.1}$	$2.1^{+0.2}_{-0.2}$	$0.21^{+0.005}_{-0.005}$	$1.14^{+0.01}_{-0.01}$	1.08 (259)
		D4	15.5 : 16.3	$1.86^{+0.2}_{-0.2}$	$1.7^{+0.2}_{-0.2}$	$0.209^{+0.005}_{-0.005}$	$1.09^{+0.01}_{-0.01}$	1.25 (251)
		D5	16.3 : 17.3	$1.82^{+0.2}_{-0.2}$	$0.9^{+0.2}_{-0.1}$	$0.205^{+0.004}_{-0.005}$	$1.0^{+0.01}_{-0.01}$	1.28 (259)
	F6	R	29.1 : 29.8	$3.6^{+0.26}_{-0.23}$	$4.7^{+0.2}_{-0.2}$	$0.198^{+0.005}_{-0.005}$	$1.51^{+0.01}_{-0.01}$	1.31 (301)
		P	29.8 : 30.2	$2.99^{+0.17}_{-0.15}$	$8.6^{+0.3}_{-0.3}$	$0.256^{+0.008}_{-0.007}$	$2.1^{+0.02}_{-0.02}$	1.17 (310)

Continued on next page

Table 3.5 – continued from previous page

Set	Flare	FS	ST:ET (ks)	kT_3 (keV)	EM_3 (10^{52} cm^{-3})	Z ($Z_\odot$)	L_{XF} (10^{30} erg s^{-1})	χ^2_ν (dof)
		D1	30.2 : 30.6	$2.99^{+0.2}_{-0.17}$	$6.6^{+0.3}_{-0.3}$	$0.247^{+0.007}_{-0.007}$	$1.84^{+0.02}_{-0.02}$	1.11 (287)
		D2	30.6 : 31.1	$3.21^{+0.22}_{-0.19}$	$5.6^{+0.2}_{-0.2}$	$0.216^{+0.006}_{-0.006}$	$1.65^{+0.01}_{-0.01}$	0.97 (289)
		D3	31.1 : 31.6	$3.27^{+0.25}_{-0.22}$	$4.6^{+0.2}_{-0.2}$	$0.201^{+0.006}_{-0.006}$	$1.49^{+0.01}_{-0.01}$	0.97 (277)
		D4	31.6 : 32.6	$2.92^{+0.2}_{-0.19}$	$4.5^{+0.2}_{-0.2}$	$0.181^{+0.006}_{-0.006}$	$1.4^{+0.01}_{-0.01}$	1.05 (268)
	F7	R1	32.6 : 34.1	$3.08^{+0.1}_{-0.1}$	$6.8^{+0.2}_{-0.2}$	$0.194^{+0.004}_{-0.004}$	$1.74^{+0.01}_{-0.01}$	1.13 (434)
		R2	34.1 : 35.1	$2.98^{+0.08}_{-0.08}$	$11.6^{+0.2}_{-0.2}$	$0.202^{+0.005}_{-0.005}$	$2.35^{+0.01}_{-0.01}$	1.03 (453)
		P	35.1 : 36.2	$2.76^{+0.06}_{-0.06}$	$14.4^{+0.2}_{-0.2}$	$0.218^{+0.005}_{-0.005}$	$2.65^{+0.01}_{-0.01}$	1.21 (488)
		D1	36.2 : 37.6	$2.51^{+0.06}_{-0.05}$	$11.2^{+0.2}_{-0.2}$	$0.224^{+0.005}_{-0.005}$	$2.25^{+0.01}_{-0.01}$	1.26 (482)
		D2	37.6 : 39.2	$2.48^{+0.06}_{-0.06}$	$8.6^{+0.2}_{-0.2}$	$0.215^{+0.004}_{-0.004}$	$1.92^{+0.01}_{-0.01}$	1.01 (460)
		D3	39.2 : 42.0	$2.31^{+0.06}_{-0.06}$	$8.0^{+0.2}_{-0.2}$	$0.197^{+0.004}_{-0.004}$	$1.77^{+0.01}_{-0.01}$	1.1 (457)
	F8	R1	42.0 : 42.9	$2.26^{+0.1}_{-0.09}$	$6.9^{+0.2}_{-0.2}$	$0.226^{+0.006}_{-0.006}$	$1.73^{+0.01}_{-0.01}$	1.02 (327)
		R2	42.9 : 43.6	$2.6^{+0.1}_{-0.1}$	$8.6^{+0.3}_{-0.3}$	$0.249^{+0.007}_{-0.007}$	$2.02^{+0.01}_{-0.01}$	1.1 (342)
		R3	43.6 : 44.2	$2.5^{+0.1}_{-0.1}$	$10.0^{+0.3}_{-0.3}$	$0.244^{+0.007}_{-0.007}$	$2.18^{+0.02}_{-0.02}$	1.08 (332)
		R4	44.2 : 44.8	$2.8^{+0.1}_{-0.1}$	$12.5^{+0.3}_{-0.3}$	$0.219^{+0.007}_{-0.007}$	$2.48^{+0.02}_{-0.02}$	1.11 (360)

Continued on next page

Table 3.5 – continued from previous page

Set	Flare	FS	ST:ET (ks)	kT_3 (keV)	EM_3 (10^{52} cm^{-3})	Z ($Z_\odot$)	L_{XF} (10^{30} erg s^{-1})	χ^2_ν (dof)
		R5	44.8 : 45.3	$3.0^{+0.1}_{-0.1}$	$16.88^{+0.4}_{-0.4}$	$0.215^{+0.008}_{-0.008}$	$3.04^{+0.02}_{-0.02}$	1.11 (376)
		P	45.3 : 45.8	$2.56^{+0.1}_{-0.07}$	$17.6^{+0.4}_{-0.5}$	$0.225^{+0.01}_{-0.009}$	$3.01^{+0.02}_{-0.02}$	1.17 (369)
		D	45.8 : 46.3	$2.42^{+0.09}_{-0.07}$	$17.4^{+0.4}_{-0.5}$	$0.257^{+0.01}_{-0.009}$	$3.04^{+0.02}_{-0.02}$	0.95 (368)
	F9	R1	46.3 : 46.7	$2.46^{+0.08}_{-0.09}$	$17.4^{+0.5}_{-0.4}$	$0.29^{+0.01}_{-0.01}$	$3.17^{+0.02}_{-0.02}$	1.0 (339)
		R2	46.7 : 47.1	$2.47^{+0.07}_{-0.08}$	$20.3^{+0.5}_{-0.5}$	$0.27^{+0.01}_{-0.01}$	$3.46^{+0.03}_{-0.03}$	1.03 (356)
		R3	47.1 : 47.4	$2.71^{+0.09}_{-0.08}$	$20.1^{+0.5}_{-0.5}$	$0.32^{+0.01}_{-0.01}$	$3.72^{+0.03}_{-0.03}$	1.24 (371)
		P	47.4 : 47.8	$2.54^{+0.07}_{-0.07}$	$20.5^{+0.5}_{-0.5}$	$0.32^{+0.01}_{-0.01}$	$3.69^{+0.03}_{-0.03}$	0.92 (366)
		D	47.8 : 48.2	$2.22^{+0.06}_{-0.06}$	$19.3^{+0.5}_{-0.5}$	$0.31^{+0.01}_{-0.01}$	$3.39^{+0.02}_{-0.02}$	1.04 (355)
S3	F10	R	39.04 : 40.49	$3.5^{+0.3}_{-0.3}$	$6.8^{+0.4}_{-0.4}$	$0.25^{+0.01}_{-0.01}$	$1.87^{+0.02}_{-0.03}$	0.88 (208)
		P	40.49 : 40.94	$3.2^{+0.2}_{-0.2}$	$16.7^{+0.7}_{-0.7}$	$0.25^{+0.02}_{-0.02}$	$3.15^{+0.04}_{-0.04}$	1.02 (230)
		D1	40.94 : 41.49	$2.5^{+0.2}_{-0.2}$	$11.2^{+0.5}_{-0.5}$	$0.28^{+0.01}_{-0.01}$	$2.34^{+0.03}_{-0.03}$	1.14 (252)
		D2	41.49 : 42.19	$2.1^{+0.1}_{-0.1}$	$7.6^{+0.4}_{-0.4}$	$0.23^{+0.01}_{-0.01}$	$1.73^{+0.02}_{-0.02}$	1.09 (228)
		D3	42.19 : 43.04	$1.8^{+0.2}_{-0.1}$	$4.8^{+0.4}_{-0.4}$	$0.23^{+0.01}_{-0.01}$	$1.39^{+0.02}_{-0.02}$	0.94 (216)
S4	F13	P	37.63 : 38.23	$2.9^{+0.1}_{-0.1}$	$14.6^{+0.5}_{-0.5}$	$0.33^{+0.02}_{-0.02}$	$2.68^{+0.03}_{-0.03}$	0.97 (268)

Continued on next page

Table 3.5 – continued from previous page

Set	Flare	FS	ST:ET (ks)	kT_3 (keV)	EM_3 (10^{52} cm^{-3})	Z ($Z_\odot$)	L_{XF} (10^{30} erg s^{-1})	χ^2_ν (dof)
		D1	38.23 : 38.63	$2.6^{+0.1}_{-0.1}$	$10.5^{+0.4}_{-0.3}$	$0.33^{+0.01}_{-0.01}$	$2.11^{+0.02}_{-0.02}$	1.15 (272)
		D2	38.63 : 39.13	$2.07^{+0.08}_{-0.1}$	$9.1^{+0.4}_{-0.3}$	$0.28^{+0.01}_{-0.01}$	$1.72^{+0.02}_{-0.02}$	1.08 (270)
		D3	39.13 :39.63	$1.67^{+0.07}_{-0.08}$	$6.7^{+0.3}_{-0.3}$	$0.28^{+0.01}_{-0.01}$	$1.4^{+0.02}_{-0.02}$	1.24 (240)
		D4	39.63 :40.23	$1.57^{+0.05}_{-0.06}$	$5.6^{+0.3}_{-0.2}$	$0.29^{+0.01}_{-0.01}$	$1.31^{+0.01}_{-0.01}$	1.14 (244)
S5	F15	R1	8.19 : 9.39	$5.7^{+0.3}_{-0.3}$	$30.0^{+0.6}_{-0.6}$	$0.29^{+0.01}_{-0.01}$	$6.40^{+0.05}_{-0.05}$	1.03 (411)
		R2	9.39 : 9.59	$7.4^{+0.3}_{-0.3}$	199^{+3}_{-3}	$0.50^{+0.04}_{-0.04}$	$38.9^{+0.3}_{-0.3}$	1.09 (561)
		R3	9.59 : 9.69	$7.7^{+0.4}_{-0.3}$	315^{+5}_{-5}	$0.53^{+0.06}_{-0.05}$	$61.5^{+0.4}_{-0.4}$	1.14 (557)
		R4	9.69 : 9.79	$6.7^{+0.3}_{-0.2}$	405^{+7}_{-7}	$0.41^{+0.06}_{-0.05}$	$73.7^{+0.6}_{-0.6}$	1.21 (472)
		R5	9.79 : 9.99	$5.8^{+0.2}_{-0.2}$	461^{+7}_{-7}	$0.40^{+0.04}_{-0.04}$	$81.0^{+0.6}_{-0.6}$	1.06 (532)
		R6	9.99 : 10.09	$5.3^{+0.2}_{-0.2}$	450^{+9}_{-9}	$0.54^{+0.06}_{-0.06}$	$80.6^{+0.7}_{-0.7}$	1.12 (432)
		P	10.09 : 10.19	$4.8^{+0.2}_{-0.1}$	491^{+9}_{-9}	$0.42^{+0.05}_{-0.05}$	$81.9^{+0.7}_{-0.7}$	1.15 (451)
S6	*F20	R	68.0 : 70.2	$2.7^{+0.3}_{-0.2}$	$47.2^{+0.6}_{-0.5}$	**	$4.80^{+0.04}_{-0.04}$	1.28 (657)
		P	70.2 : 71.5	$2.07^{+0.05}_{-0.08}$	132^{+1}_{-1}	**	$12.19^{+0.08}_{-0.09}$	1.35 (906)
		D1	71.5 : 73.3	$1.97^{+0.03}_{-0.03}$	$92.4^{+0.7}_{-0.7}$	**	$8.84^{+0.06}_{-0.06}$	1.76 (925)

Continued on next page

Table 3.5 – continued from previous page

Set	Flare	FS	ST:ET (ks)	kT_3 (keV)	EM_3 (10^{52} cm^{-3})	Z ($Z_\odot$)	L_{XF} (10^{30} erg s^{-1})	χ^2_ν (dof)
		D2	73.3 : 76.2	$1.79^{+0.02}_{-0.02}$	$55.1^{+0.5}_{-0.5}$	**	$5.57^{+0.04}_{-0.04}$	1.95 (962)
		D3	76.2 : 81.1	$1.68^{+0.03}_{-0.03}$	$27.8^{+0.3}_{-0.3}$	**	$3.16^{+0.02}_{-0.02}$	1.90 (947)
		D4	81.1 : 90.3	$1.65^{+0.03}_{-0.06}$	$10.7^{+0.1}_{-0.1}$	**	$1.62^{+0.01}_{-0.01}$	1.62 (948)

* Spectral fitting was carried out using RGS spectra.

** The abundances were fixed to the quiescent state values of segment P11.